Supplementary Information

Section 1: Laser source

The source generates a linearly polarized laser with 1.5 mJ energy, 800 nm central wavelength, and 35 nm bandwidth from a Ti:Sapphire amplifier system at 3 kHz repetition rate that is coupled into an Ar-filled hollow-waveguide, where it undergoes spectral broadening up to 130 nm FWHM bandwidth due to self-phase modulation[6]. The waveguide is 1 m long with 500 μm core diameter. The CEP of the input pulses can be locked within 200 mrad rms. We actively control the pointing of the input pulses for short- and long-term stability, exhibiting <0.5% rms of intensity fluctuations over several hours of operation.

Table 1: Relevant laser parameters at and far from the interaction point

	Far-field	At IP
Central wavelength	810 nm	
Bandwidth	135 nm FWHM	
Pulse duration	8 fs FWHM-Gauss	
Energy	0.85 mJ	0.6 mJ
Repetition rate	3 kHz	
Waist	-	1.2 μm $1/e^2$
Divergence	5 mrad	-
Intensity fluctuations	<0.5%	
Uninterrupted operation	>48 hrs	
Polarization	93% radial	
Beam mode	Annular-Gaussian	Axial-Gaussian

The beam polarization state is converted from linear to radial employing a highly-efficient low-dispersion broadband segmented achromatic waveplate consisting of eight λ/2 retarders over the entire broadened pulse bandwidth. The birefringence of each segment is aligned so that the beam transverse field vectors become cylindrically symmetric. We achieve a measured polarization purity higher than 93%. The pulses are compressed to a near transform-limited duration of 8 fs by employing a suitable set of dispersive optics with total second and third order dispersions of 320 fs^2 and 210 fs^3, respectively.

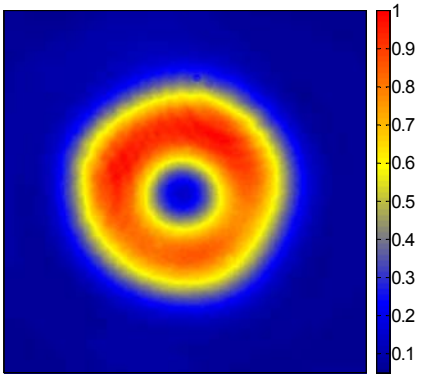

Figure 5 | Few-cycle radially polarized beam. Far-field intensity distribution of high-purity TM_{01}-mode beam. Beam diameter in the image is 8 mm with 5 mrad divergence.

Section 2: DC gun, interaction chamber, and detection system

The monoenergetic electron bunch is generated from a photocathode excited by a small portion of the radially polarized beam and accelerated via a 40 kV DC gun. The focusing solenoid is 4.45 mm thick, has a radius of 2.75 mm, and is located 24.8 mm from the photocathode. The 90-degree off-axis parabola used to focus the laser beam is 25.4 mm in diameter with a 25.4 mm effective focal length (NA=1), has a 1 mm through-hole and is located a few mm off the exit of the solenoid. A pinhole was drilled by the laser source *in situ* and located for alignment near the interaction point to ensure maximal overlap between both transverse orthogonal dimensions of the bunch and the laser beam. The magnetic dipole is located 10 cm away from the interaction point. The distance between the deflector and the micro-channel plate is 18 cm. The footprint of the entire interaction chamber is no larger than 0.5 m^2.

Table 2: Electron beam parameters per bunch, instrumentation, and detection

Initial kinetic energy	40 keV
Energy spread	250 eV
Bunch length	1 mm
Bunch charge	5 fC
Exposure time	60 seconds
Events per exposure	180000
Vacuum	$<5x10^{-6}$ Torr
Magnet dipole strength	~100 Gauss
Nominal resolution	100 eV/pxl
Pixel size	25.4 µm

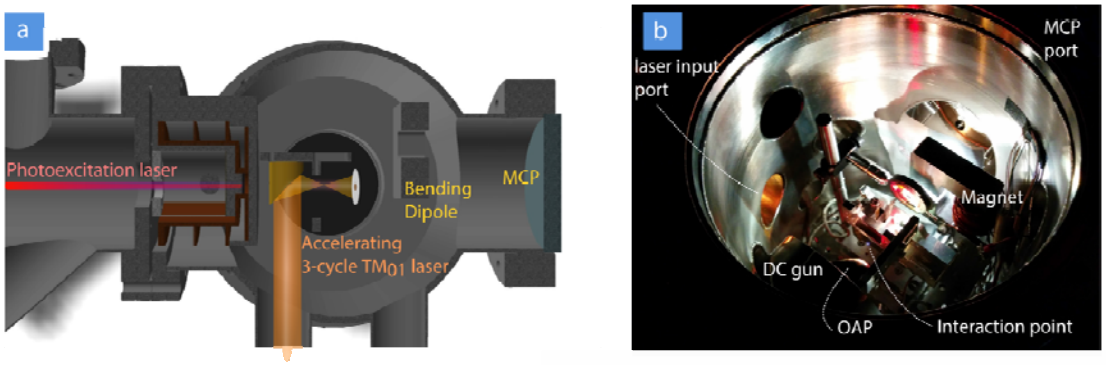

Figure 6 | Experimental setup. a) To-scale drawing of DC gun, interaction chamber, and detection. b) Laser alignment in the interaction chamber under atmospheric conditions.

Section 3: Data acquisitions and analysis

Each of the experimental data points is calculated directly from three subsequent recordings. Each recording contains two independent 60 second long exposures at 3 kHz repetition rate.

1. Recording 1: Electron beam without interaction. Cathode laser is on, driving laser is off. Two independent acquisitions with $1.8 \cdot 10^5$ events each.
2. Recording 2: Electron beam with interaction. Cathode laser is on, driving laser is on. Two independent acquisitions with $1.8 \cdot 10^5$ events each.
3. Recording 3: Background signal. Cathode laser is off, driving laser is on. Two independent acquisitions with $1.8 \cdot 10^5$ events each.

Recording 1 serves to simultaneously monitor the electron beam properties, avoid slow laser drifts, verify repeatability, and correlate interaction events to most recent electron beam without interaction. Recording 2 displays raw electron beam recordings arising from the interaction with the driving laser, which include an energy redistribution map of the electron bunch and an increased background level due to photon scatter. Recording 3 is used to remove the photon scatter from the energy distribution maps in Recording 2. Each of the recordings is acquired in two independent subsets in order to rule out non-repeatable events arising from ambient instabilities.

Section 4: Electric field distribution near and at the focal plane

We model the pulsed, radially-polarized laser beam with an exact, singularity-free solution to Maxwell's equation. The electric field distribution of the transverse and longitudinal components is shown in Fig. 7 at three different times: 3 cycles before arriving at the focal plane (τ=-8fs); at the focal plane (τ=0fs); and 3 cycles after arriving at the focal plane (τ=8fs). Only the electrons on-axis at maximum longitudinal electric field overlap (Fig. 7.e) will experience pure direct on-axis acceleration. The majority of the electrons in all other possible phases will interact with both transverse and longitudinal fields. Some initially off-axis electrons will be drawn towards the optical axis due the transverse field confinement.

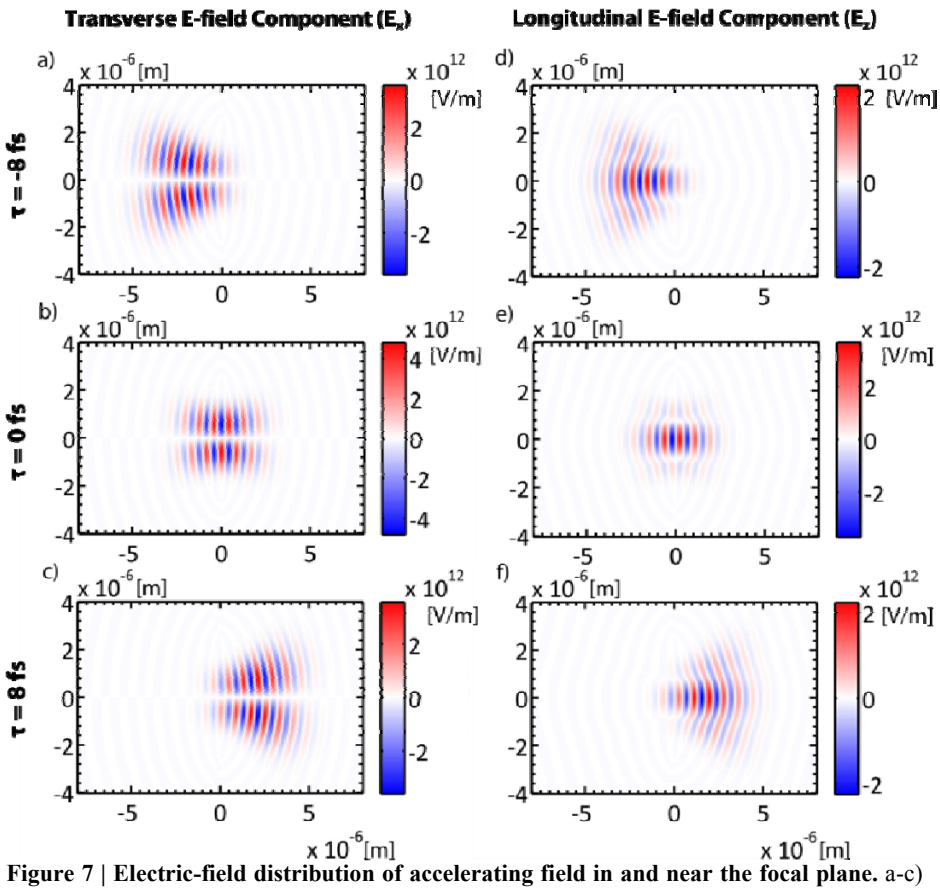

Figure 7 | Electric-field distribution of accelerating field in and near the focal plane. a-c) Transverse electric field component (E_x) strength at τ = -8, 0, 8 fs, where τ = 0 indicates the time of maximum intensity (focal plane). Cylindrical symmetry of the transverse vector field distribution is assumed (E_y=E_x). d-f) Longitudinal electric field component (E_z) strength at τ = -8, 0, 8 fs.

Section 5: Particle tracking model

We perform simulations using a particle-tracking program. We solve the Lorentz force equation for each particle via an adaptive-step fifth-order Runge-Kutta algorithm. The particles are uniformly distributed in an ellipsoid of semi-principal axes of length 5 μm and 4 μm in the transverse and longitudinal dimensions, respectively, in order to restrict our attention to particle dynamics in the interaction volume. The coordinates of each particle are assigned in a quasi-random fashion using Sobol sequences. In this model, the electrons start off with an initial energy of 50 keV in field-free vacuum and interact with the 0.6 mJ, 8 fs pulse close to the focal plane of the near-λ focused beam.

Fig. 8 shows a $4 \cdot 10^5$-particle distribution long after (10 ps) interaction. Fig. 8.a shows a net kinetic energy gain of up to 450 keV from direct field acceleration but of a few particles only. Fig. 8.b shows the spatial distribution of this particle bunch, where a significant fraction of the electrons undergo strong ponderomotive acceleration and exhibit non-zero azimuthal angle. Fig. 8.c complements the simulation set by illustrating the final particle kinetic energy with respect to azimuthal (off-axis deflection) angle. The electrons on axis (zero deflection angle) are the result of direct acceleration from the Lorentz force exerted by the longitudinal field components on axis. Here, only a few electrons (approximately 1 in 10^5) are accelerated to quasi-relativistic speeds exclusively due to direct on-axis acceleration.

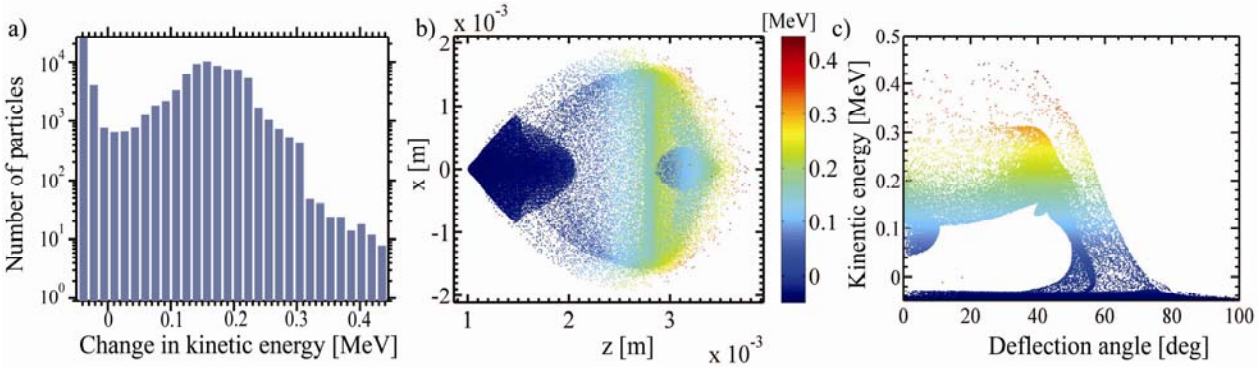

Figure 8 | Expected particle distribution after interaction. a) change in kinetic energy distribution of 10^5 particles; b) spatial distribution along longitudinal axis (z) with transverse symmetry (x) of the bunch 20 ps after laser collision; c) deflection angle distribution corresponding to data in b).

Section 6: Particle distribution under experimental constraints

In our study, we are interested in detecting the electrons that are pushed in the forward direction (longitudinally) with nearly zero deflection angle. This is experimentally carried out by limiting the acceptance half-angle of the accelerated electrons entering the electron spectrometer to 25 mrad (1.43°). Therefore, the electron spectrum being detected is that contained in the 0° - 1.43° range of Fig. 8.c, while the highest detectable electron energy range is limited by signal-to-noise ratio. This limit only reaches up to approximately 30% above the initial electron energy and arises from the dimension mismatch of the relativistic laser Rayleigh-volume (0.8μm×2.5μm×2.5μm) relative to the electron bunch volume (1mm×0.25mm×0.25mm).

In the model we restrict our attention to the accelerated electron bunch within 25 mrad deflection angle. The corresponding distribution (Fig. 9) resembles the conditions imposed experimentally. The expected divergence distribution illustrated in Fig.3 is directly computed from the distribution in Fig. 9. The azimuthal electron count distribution matches the measurements shown in Fig. 2.b, and demonstrates that the detected charge is highly directional on axis.

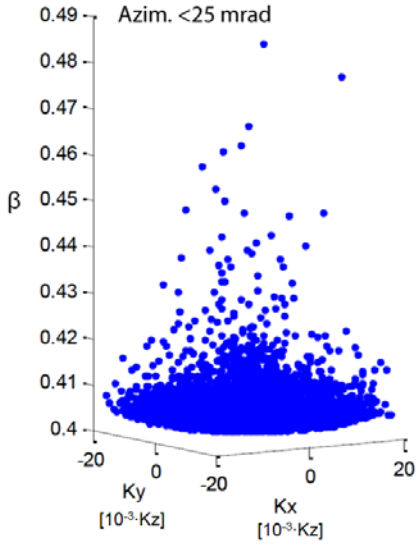

Figure 9 | Simulated normalized velocity of longitudinally accelerated electrons with <25 mrad deflection angle. Distribution of relativistic β ($\beta = v/c$) corresponding to the electron kinetic energy range from 40 keV to 60 keV as a function of transverse k-vector distribution where $k = 2\pi/\lambda$ for electrons with less than 25 mrad half-angle divergence off axis.